

The sdA problem – III. New extremely low-mass white dwarfs and their precursors from *Gaia* astrometry

Ingrid Pelisoli^{1,2*}, Keaton J. Bell^{3,4}, S. O. Kepler², D. Koester⁵

¹*Institut für Physik und Astronomie, Universitätsstandort Golm, Karl-Liebknecht-Str. 24/25, 14467 Potsdam, Germany*

²*Instituto de Física, Universidade Federal do Rio Grande do Sul, 91501-900, Porto-Alegre, RS, Brazil*

³*Max-Planck-Institut für Sonnensystemforschung (MPS), Justus-von-Liebig-Weg 3, 37077 Göttingen, Germany*

⁴*Department of Physics and Astronomy, Stellar Astrophysics Centre, Aarhus University, Ny Munkegade 120, 8000 Aarhus C, Denmark*

⁵*Institut für Theoretische Physik und Astrophysik, Universität Kiel, D-24098, Kiel, Germany*

Accepted XXX. Received YYY; in original form ZZZ

ABSTRACT

The physical nature of the sdA stars—cool hydrogen-rich objects with spectroscopic surface gravities intermediate between main sequence and canonical mass white dwarfs—has been elusive since their discovery in Sloan Digital Sky Survey Data Release 12 spectra. The population is likely a mixture of A/F stars in the halo with overestimated surface gravities, and extremely low-mass white dwarfs and their precursors, i.e., ELMs and pre-ELMs. In this work, we seek to identify (pre-)ELMs with radii smaller than is possible for main sequence stars, allowing even for very low metallicity. We analyse 3891 sdAs previously identified in the Sloan Digital Sky Survey using *Gaia* DR2 data. Our Monte Carlo analysis supports that 187 of these are inconsistent with the main sequence, which we interpret as likely (pre-)ELMs given their spectral class. Of these, 66 pass more conservative criteria that allow for higher systematic uncertainties on the spectroscopic temperature or parallax, as well as an approximate treatment of extinction. Our identifications increase the number of known (pre-)ELMs up to threefold, demonstrating how *Gaia* astrometry can reveal members of the compact (pre-)ELM subpopulation of the sdA spectral class.

Key words: subdwarfs – white dwarfs – binaries: general – stars: evolution

1 INTRODUCTION

The spectroscopic class of subdwarf A stars (sdAs) was proposed by Kepler et al. (2016) to refer to thousands of hydrogen-rich objects in the Sloan Digital Sky Survey (SDSS) whose surface gravities derived from their low resolution spectra could not be explained by single-star evolution models. They show temperatures below the zero-age horizontal branch (ZAHB), $7000 \lesssim T_{\text{eff}} < 20000$ K (most $\lesssim 10000$ K), and $\log g$ intermediate between main sequence A stars and hydrogen-atmosphere (DA) white dwarfs resulting from single evolution, $4.5 \lesssim \log g \lesssim 6.0$. They were unveiled among stars identified as O, B, and A type by the SDSS pipeline. Early-type main sequence stars in SDSS are more distant than ≈ 8 kpc to be below the saturation limit ($g \approx 14.0$), or essentially in the halo, given that SDSS observes mostly outside of the disc. As the halo is over 10 Gyr old and the main sequence lifetimes of these spectral classes is shorter than 1.5 Gyr, we do not expect a scattered large population of early-type stars in SDSS.

The initial suggestion of Kepler et al. (2016) was that the sdAs could be extremely-low mass white dwarfs (ELMs) missed by the selection criteria of the ELM Survey (Brown et al. 2010; Kilic et al. 2011; Brown et al. 2012; Kilic et al. 2012; Brown et al. 2013; Gianninas et al. 2015; Brown et al. 2016). ELMs show masses below the single-star evolution limit for white dwarfs of $M \approx 0.3 M_{\odot}$ ($\log g \approx 6.0$). The Universe is not old enough for low mass stars to have evolved off the main sequence and turned into $M \lesssim 0.3 M_{\odot}$ white dwarfs (e.g. Kilic et al. 2007). However, over 50 per cent of stars with $M \gtrsim 1 M_{\odot}$ are in binaries (Duchêne & Kraus 2013), and about 25 per cent are close enough to interact (Willems & Kolb 2004), potentially leading to a common envelope phase. The friction between the pair of stars and the envelope can lead to envelope ejection, causing significant mass loss and bringing the binary stars closer together. This is believed to be the main channel of ELM formation (e.g., Marsh et al. 1995; Nelemans et al. 2001).

The ELM Survey selected mostly hot ($T \gtrsim 10000$ K), $M \gtrsim 0.15 M_{\odot}$ ELMs. Moreover, they considered the detection of a close binary companion as a requirement for

* E-mail: ingrid.pelisoli@ufrgs.br

a clear ELM classification (Brown et al. 2016). Whereas common-envelope evolution is thought to be the main formation channel for ELMs, alternative formation scenarios include the merger of the inner binary in a hierarchical triple system (Vos et al. 2018), supernova stripping (Wang & Han 2009), and mass ejection caused by a massive planet (Nelemans & Tauris 1998). Therefore, the existence of single ELMs should not be ruled out. The ELMs can give us important clues as to the evolution of compact binary systems and of hierarchical triple systems, which are still poorly understood (e.g. Postnov & Yungelson 2014; Toonen et al. 2016), hence an unbiased-sample would be a valuable asset to testing evolution and population synthesis models.

The ELM explanation for the sdAs was questioned by Brown et al. (2017) and Hermes et al. (2017). Hermes et al. (2017) relied on the radial velocities estimated from SDSS subspectra and concluded that the vast majority of the sdAs published by Kepler et al. (2016) (> 99 per cent) were not in close binaries, and therefore that they could not be ELMs. Other formation channels such as mergers were excluded due to the low proper motion of most of the sdAs published in Kepler et al. (2016). Brown et al. (2017) suggested that sdAs were predominantly metal-poor A/F main sequence stars in the halo, arguing that the number of sdAs was far too large compared to the predicted number of cool ELMs given the density of objects estimated from the known sample. They also studied six eclipsing binaries in the sample, and found their radii to be too large for compact objects. The possibility that the objects are in the pre-ELM phase, before the stars reach the cooling branch and still show extended radii (e.g., Maxted et al. 2011; Rappaport et al. 2015), was not seriously considered, perhaps because the lifetimes in those phases are short. Brown et al. (2017) also suggested that the use of pure-hydrogen models caused the $\log g$ values of Kepler et al. (2016) to be overestimated.

In Pelisoli et al. (2018a), we showed that metallicity could not be responsible for a systematic overestimate of $\log g$. Some values of $\log g$ could even be underestimated by the pure-hydrogen models. Moreover, we found no dependence with metallicity for the difference between our $\log g$ values and those estimated by the SEGUE stellar parameter pipeline (SSPP, Lee et al. 2008). Importantly, it became clear that the sdAs were composed of overlapping stellar populations, given a bi-modal distribution in $(g - z)$. This result was corroborated by Bell et al. (2018), who found that the sdAs show varied pulsation spectra that cannot be explained with a single population. We obtained another interesting result in Pelisoli et al. (2018b) by comparing the $\log g$ obtained from SDSS spectra with values derived from ESO X-shooter high resolution spectra. The SDSS values for the four stars observed were larger by 1 dex, which could be explained by the lack of spectral coverage below 3700 Å and low resolution in the SDSS spectra, considering that the width of the lines show little dependence on $\log g$ for temperatures in the sdA range. This could potentially explain the inconsistency raised by Brown et al. (2017).

Clearly the SDSS spectra and colours are not enough to uniquely determine the nature of the sdA stars. They could be binary byproducts, holding the potential to shed light on the evolution of multiple systems, or main sequence stars in the halo, which could illuminate the structure and formation history of the Galaxy. Resolving their nature is

therefore advantageous in both aspects. With parallax measurements from data release 2 of *Gaia*, we can place constraints on the radii of these objects, making their nature clearer. In this work, we explore the nature of the sdAs in light of *Gaia* DR 2 data. In particular, we seek to identify sdAs that must be (pre-)ELMs based on radius constraints from *Gaia* astrometry.

2 DATA ANALYSIS

We focused our analysis on objects from sample A of Pelisoli et al. (2018a), which were selected among stars with SDSS pipeline classifications of O, B, and A for which we obtained good spectroscopic fits (38 850 objects). We also analyse objects in tables 1 and 2 of that work in particular. The former are objects whose SDSS spectra yield $\log g > 5.5$ when fit with solar-abundance spectral models. The latter were objects found to be more likely (pre-)ELMs than main sequence stars given a probabilistic analysis that took into account the $g - z$ colours, spatial velocities (U, V, W), and the fitted $\log g$ values compared to both single (Bertelli et al. 2008, 2009) and binary evolution models (Istrate et al. 2016).

We retrieved their coordinates (α, δ), parallaxes (π), proper motions (μ_α and μ_δ), and magnitudes in the G, G_{BP} and G_{RP} passbands from the *Gaia* DR2 catalogue, as well as quality control parameters, using the coordinates from SDSS and a 3" search radius. For 490 objects there were multiple identifications within this radius; we selected the *Gaia* source closer to the SDSS coordinates, being left with identifications for 38 825 objects within 3". All but two of the unmatched sources correspond to spectra taken at the position of diffraction rays of bright stars by the SDSS. One of the remaining two could be recovered with a 5" radius, but the other returned no match even with a 15" radius.

2.1 Filtering

Although impressive and holding potential to revolutionise astronomy, *Gaia* data are not perfect; thus, filtering is required to avoid contamination of spurious measurements or outliers. In order to obtain a set of filtering parameters adequate to our sample, allowing us to identify true (pre-)ELMs within the sdAs, we analysed the *Gaia* data of the 76 binary ELMs of Brown et al. (2016) considering the criteria outlined in Appendix C of Lindegren et al. (2018). As can be seen in Fig. 1, all the known ELMs obey the selection suggested by Lindegren et al. (2018) in terms of the accuracy of the astrometric solution unit weight error, $u = \sqrt{\text{astrometric_chi2_al}/(\text{astrometric_n_good_obs_al} - 5)}$

$$u < 1.2 \times \max(1, \exp(-0.2(\text{phot_g_mean_mag} - 19.5))) \quad (1)$$

with the exception of SDSS J093506.92+441107.0, a double WD binary with a period of 20 minutes that appears to have an M dwarf along the line of sight (Kilic et al. 2014) that probably affected the *Gaia* solution. We thus adopted the same filtering criterion as Lindegren et al. (2018) on u .

The next criterion suggested by Lindegren et al. (2018) to obtain a clean sample relies on the flux excess factor $E = (I_{BP} + I_{RP})/I_G$ ($\text{phot_bp_rp_excess_factor}$), where I_X is the photometric flux in the band X (Evans et al. 2018).

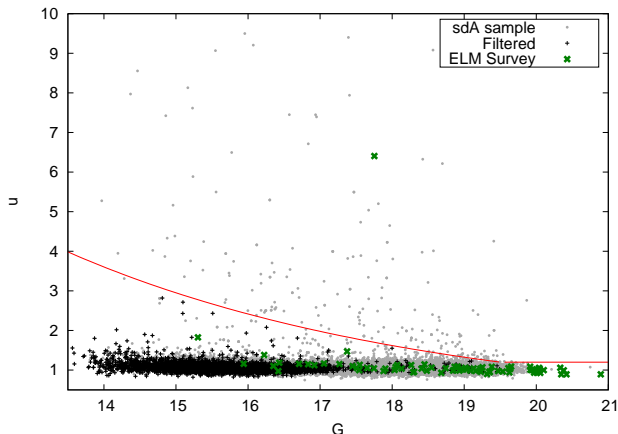


Figure 1. Accuracy of the astrometric solution unit weight $u = \sqrt{\chi^2/(\nu - 5)}$ as a function of the apparent magnitude G for the sdA sample (grey) and known ELMs (green crosses). The analysed sdA sample, after all filtering criteria were applied, is marked in black. The red line represents the upper limit defined by Lindegren et al. (2018) for good quality data.

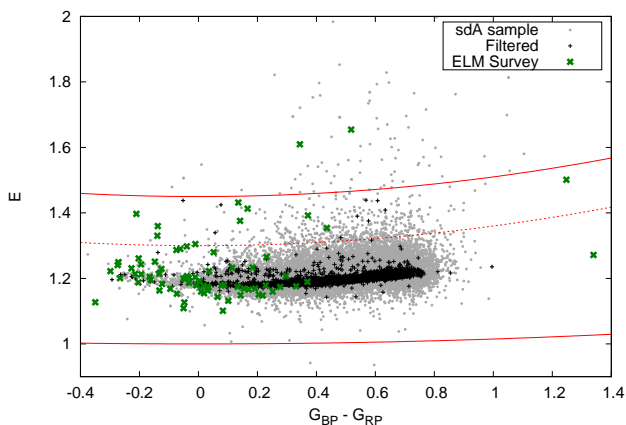


Figure 2. Flux excess factor as a function of colour, with the same colour-code as Fig. 1. The solid red lines represent our adopted selection, which uses the same lower limit as Lindegren et al. (2018). The dashed line is the upper limit set by Lindegren et al. (2018), which excludes a large fraction of the known ELMs.

As shown in Fig. 2, the selection of Lindegren et al. (2018) excludes many known ELMs (about 15 per cent). This is probably due to the fact that ELMs are binaries, so that the flux of the (cool) unseen secondary star might affect the measurement of I_{RP} and cause an excess. Therefore, we relaxed the arbitrary cut of Lindegren et al. (2018) to include a larger fraction of the known ELMs, adopting as a cut

$$1.0 + 0.015(G_{BP} - G_{RP})^2 < E < 1.45 + 0.06(G_{BP} - G_{RP})^2, \quad (2)$$

which includes 97 per cent of the ELMs; only SDSS J081822.34+353618.9 and J100554.05+355014.2 are outside the selected region.

Considering the size of the sample, we further restrict our selection to include objects showing uncer-

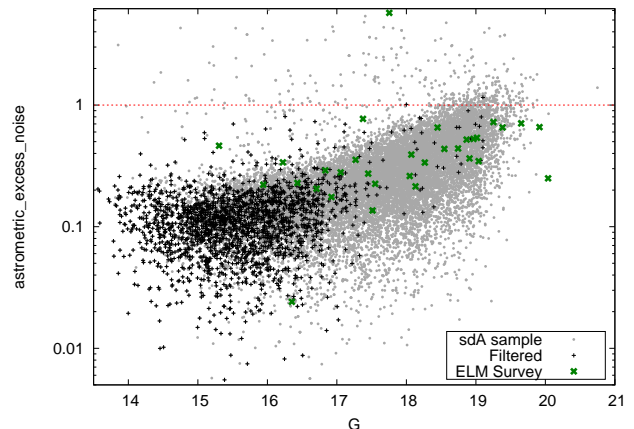


Figure 3. Astrometric excess noise as a function of magnitude. Colours for the symbols are the same as in Fig. 1. The dashed line marks the position of astrometric excess noise equal to 1 mas.

tainty in the parallax smaller than 25 per cent, i. e. $\text{parallax_over_error} > 4$, excluding about 90 per cent of our initial sample (sample A of Pelisoli et al. 2018a). This $4\text{-}\sigma$ cut suggests (assuming Gaussian uncertainties) that fewer than three stars in our analysed sample have spurious parallax detections. We caution that a similar cut in the sample of known ELMs would exclude more than 60 per cent of the objects.

The outlined selection criteria have also excluded from our sample objects with high $\text{astrometric_excess_noise}$, a parameter that quantifies how much the solution deviates from the single-source solution adopted by Gaia. The binarity of the ELMs is of course expected to cause deviations; however, as the binaries are too close to be resolved by Gaia, they should still be relatively well modelled by a single-star solution, as can be noted from Fig. 3. The only known ELM that shows high noise is SDSS J093506.92+441107.0, which was also an outlier in the u selection.

Removing double identifications (objects with more than one observation in the SDSS, with slightly different coordinates), we are left with 3891 unique identifications obeying our selection, which we will refer to as the “reliable π ” sample throughout the text. We note that this subsample is biased to include smaller stars at a given magnitude, as we expect nearer sources to have higher signal-to-noise parallax measurements.

2.2 Radii estimates

We estimate the radii of the sdAs that are required to bring the observed magnitudes, effective temperatures, and parallaxes into agreement, largely following the approach of Andrae et al. (2018), with a few improvements. First, we have obtained effective temperatures by fitting SDSS spectra and selecting the solution that best agrees with SDSS and GALEX photometry, allowing for a more accurate determination than that solely based on Gaia photometry as done by Andrae et al. (2018). Moreover, we propagate uncertainties in all variables via Monte Carlo, rather than the simple first-order approximation adopted by Andrae et al. (2018), which also neglects the effect of the luminosity uncertainty

in the radius. The steps of our estimates are described in more detail below.

We subtracted the zero-point of $-29 \mu\text{as}$ from the parallaxes (Lindgren et al. 2018) of all matched objects. This zero-point was determined from quasars, which have similar colours to white dwarfs and A-type stars, hence it should be adequate for our sample. There is, however, a dependence of the magnitude of this zero-point with colour, and it can be larger for cooler objects such as the sdAs (see e.g. Zinn et al. 2018). A greater negative zero-point would imply larger parallax, which in turn implies smaller distance and therefore smaller radius. Thus our assumption of a $-29 \mu\text{as}$ zero-point could cause our radii to be slightly overestimated. As we are searching the objects with radii smaller than main sequence, this can be considered a conservative zero-point.

We estimated the distance d , absolute magnitude M_G , bolometric magnitude M_{bol} , luminosity $\log(L/L_\odot)$, and radius R/R_\odot for each object with a Monte Carlo simulation, taking into account the uncertainties in the value of the parallax π . The uncertainties in the G magnitude, and in T_{eff} (initially assumed to be equal to the external uncertainty of 5 per cent; Pelisoli et al. 2018a,b) are also propagated. Expected values were taken to be the medians of each distribution, whereas upper and lower uncertainties were taken to be the 16th and 84th percentiles, yielding an interval of confidence of 68 per cent.

The distance d for each individual source was estimated from the distribution of $(\pi')^{-1}$, where π' is the parallax corrected for the zero point—an improvement compared to the simple inversion of parallax employed by Andrae et al. (2018). We opted not to use any priors due to the fact that, as shown by Pelisoli et al. (2018a) and Bell et al. (2018), the sdAs are composed by multiple populations, hence no single prior would be adequate to the whole sample. This choice can somewhat bias the distance estimate, especially for distant stars ($d \gtrsim 2$ kpc), whose distribution might show an extended tail to unphysically large distances (Bailer-Jones 2015; Luri et al. 2018). However, the impact of this is mitigated by the fact that we only analyse objects with small fractional parallax uncertainty ($\sigma_\pi/\pi < 0.25$). In fact, our distance estimates show very good agreement up to ≈ 1.5 kpc with the estimates of Bailer-Jones et al. (2018), who assumed an exponentially decreasing space density prior in distance. Above 1.5 kpc, our distances are somewhat larger, which will cause larger radii estimates compared to what we would obtain by using a single prior. This choice again errs on the side of caution in our effort to identify (pre-)ELMs among the sdA stars.

The absolute magnitude for each source was calculated as

$$M_G = G + 5 \log \pi' + 5. \quad (3)$$

We do not account for extinction at this moment, given that the extinction in the *Gaia* archive is not recommended for the analysis of stars individually (Andrae et al. 2018). The effect of neglecting extinction is discussed below. We applied the bolometric corrections given in table 12 of Jordi et al. (2010) to obtain M_{bol} . As the external uncertainty in the $\log g$ that we derived from SDSS spectra is quite high (about 0.5 dex, see discussion in Pelisoli et al. 2018b) and we do not have high resolution spectra to accurately determine the metallicity, we assume the average bolometric

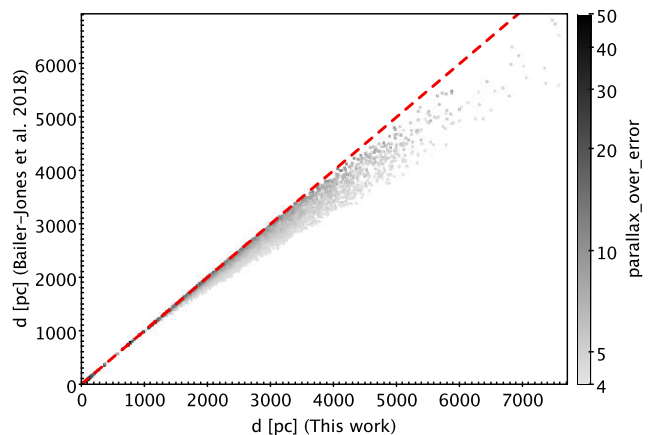


Figure 4. Comparison between our estimated distances and those of Bailer-Jones et al. (2018), colour-coded by the parallax over error parameter. The dashed red line represents equality. For nearby objects ($d \lesssim 1.5$ kpc), there is remarkable agreement. Above this, our distances are somewhat larger than those of Bailer-Jones et al. (2018).

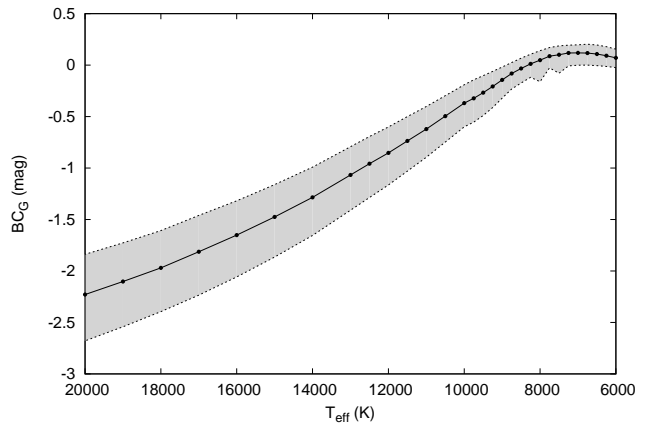


Figure 5. The black points show the average values of the bolometric correction to M_G for each T_{eff} (Jordi et al. 2010). They give a smooth function represented by the solid line, hence the bolometric correction can be estimated from interpolation given the T_{eff} . The dashed lines represent the minimum and maximum value for each T_{eff} .

correction given the effective temperature (which we estimated to have an uncertainty smaller than 5 per cent when derived from the SDSS spectra, see Pelisoli et al. 2018a,b), with the uncertainty taken to be the difference between either the minimum or the maximum value and the average — whichever was larger. As can be seen in Fig. 5, the bolometric correction does not have a large dependence on $\log g$ and metallicity in the temperature range of the sdAs, so the uncertainties from this method are only on the order of 0.5 mag, still they were also propagated in our simulations. Using the bolometric magnitude, we calculated $\log(L/L_\odot)$ from

$$\log\left(\frac{L}{L_\odot}\right) = \frac{4.74 - M_{\text{bol}}}{2.5}. \quad (4)$$

The radius of each object was finally obtained by using

the Stefan-Boltzmann law relating L , T_{eff} and R . The main sources of uncertainty in this method are the bolometric correction and the extinction.

To estimate the effect of the bolometric correction, we calculated a second set of radii estimates independent of the bolometric correction, by using the solid angle obtained as part of our photometric fit to each object. As the spectroscopic fit can show degenerate solutions with similar χ^2 , we first fit the photometry with stellar models that assume a fixed $\log g = 4.5$ so that we can select the spectroscopic solution whose temperature is consistent with the photometry. The ratio between the observed and modelled photometric brightness is related through the solid angle, which is proportional to $(R/d)^2$. Hence, the radius can be estimated given the distance. In this case the main uncertainty is only the extinction correction. We applied the full-correction from the maps of [Schlegel et al. \(1998\)](#), which have a resolution of only $4'$, to the *ugriz* magnitudes previous to our photometric fit. The radius estimates from the two methods were not consistent within 3σ for only 53 objects (1.6 per cent), suggesting that the bolometric correction has no large effect. Henceforth we use the estimate from the luminosity, which is independent from our fit to the SDSS photometry.

Neglecting the extinction correction can cause the distances and radii to be underestimated, a major concern given that we are interested in finding the objects with radii smaller than main sequence. To estimate the effect of a lack of extinction correction, we made a third calculation of radii obtaining the apparent Gaia magnitude G from the SDSS filters g and i using the transformations of [Evans et al. \(2018\)](#), and correcting extinction in both SDSS filters following [Schlegel et al. \(1998\)](#). We consider how this correction affects our (pre-)ELM identifications in Section 3.

Another concern is the systematic uncertainty in the *Gaia* parallax, which is about 0.1 mas ([Luri et al. 2018](#)). To verify the effect of this on our radii estimates, we validate those identifications of (pre-)ELMs that remain inconsistent with the main sequence after quadratically adding this to the uncertainties reported in the catalogue.

Given the *Gaia* five-parameter astrometric solutions, we have also computed the galactic coordinates X, Y, Z and spatial velocities U, V, W for each of our targets following [Johnson & Soderblom \(1987\)](#). Given that they are too faint to have radial velocity estimates from *Gaia*, we have relied on the radial velocities that we estimated from their SDSS spectra. Our estimates derived from the hydrogen lines show very good agreement with the estimates from the SDSS pipeline, within an average uncertainty of 20 km/s.

The radial velocity variations between SDSS subspectra of the objects in this sample were also analysed. These amplitudes were calculated with the approach described in [Pelisoli et al. \(2017\)](#), which was based on the work of [Badenes & Maoz \(2012\)](#). It consists of fitting a Gaussian to each of the Balmer lines in the normalized spectra to determine the line centre, then using this value to compute a radial velocity for each line. The radial velocity of the object at the epoch of each spectrum is calculated to be the average velocity over all the lines. We then calculate the difference between minimal and maximal velocities for each object, which is a proxy for the amplitude of radial velocity variation. We obtained good fits to the subspectra of 3664 objects in the sample.

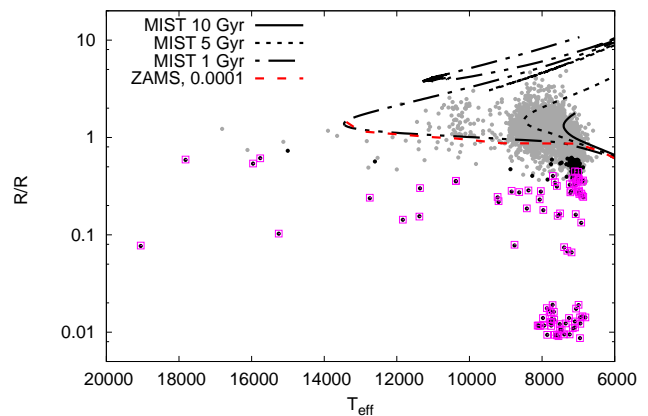


Figure 6. Radius as a function of T_{eff} for all objects with reliable parallax. The red line shows the zero-age main sequence (ZAMS) for the indicated metallicity ([Romero et al. 2015](#)). The black lines show the radii from MIST isochrones ([Dotter 2016](#); [Choi et al. 2016](#)) for $[\text{Fe}/\text{H}] = -4$. The objects showing radii smaller than the minimum main sequence radius, taking into account a 99 per cent confidence interval and assuming a 5 per cent uncertainty in T_{eff} , are shown as black points. Magenta squares mark the objects which are still below the main sequence when 10 per cent in T_{eff} uncertainty is assumed.

3 RESULTS

The main candidate explanations put forward for the sdAs are A/F main sequence stars in the halo ([Brown et al. 2017](#)), and (pre-)ELMs ([Pelisoli et al. 2018a](#)). The main difference between these two evolutionary classes is their radii. A/F main sequence stars show $R \gtrsim 0.6 R_{\odot}$, depending on T_{eff} , even for very low metallicity (e.g. $z \approx 10^{-4}$, see Fig. 6). With larger metallicity, the radius is larger because of the increase in opacity. Evolution off the main sequence also causes the radius to increase, due to thermal energy being released by the contracting nucleus. Hence, the zero age main sequence (ZAMS) radius for low metallicity is the conservative minimal radius for a main sequence star at a given T_{eff} . (Pre-)ELMs, on the other hand, have $R \lesssim 0.1 R_{\odot}$ during most of their evolution. The radius of a pre-ELM can nonetheless be larger because of residual burning (e.g., the RR Lyra found by [Pietrzyński et al. 2012](#)). Although the time spent in these burning stages is short, the objects are much brighter, hence they have considerable chances of being detected ([Pelisoli et al. 2018a](#)). In short, (pre-)ELMs can show radii in an extensive range, but main sequence stars have a minimal radius.

We have used this minimal radius to investigate which objects in our sample could not be explained as main sequence stars. Using the radii estimated from the parallaxes, we verified whether each star was smaller than the ZAMS at the estimated T_{eff} considering the 99 per cent confidence interval of our Monte Carlo simulation—i.e. 99 per cent of the simulated radii had to be below the minimum radius at the best-fit T_{eff} for it to be considered smaller than the ZAMS. From the sample of 3891 objects, we found 234 showing $R_{99\%} < R_{\text{ZAMS}}$, highlighted in Fig. 6. Objects with radii below the ZAMS cannot be main sequence stars. Removing canonical mass white dwarfs with spectral types other

than pure A (e.g. with helium contamination or magnetic fields, which affect the $\log g$ estimate), we are left with 187 objects. Considering their spectral class, these are high-probability compact objects. These 187 targets are listed in Table 1, except for two previously known ELMs published by Brown et al. (2016) (SDSS J123800.09+194631.4 and SDSS J155502.00+244422.0). Another 41 objects were previously classified as white dwarfs (mostly by Kleinman et al. 2013), but only fitted with models with $\log g > 5.0$, whereas our grid extends down to $\log g = 3.5$.

In Fig. 7, we show the H-R diagram for our reliable parallax π sample. Single and binary evolution models are over-plotted. The position of the objects for which we determine the radius to be smaller than the main sequence agrees quite well with the binary evolution models of Istrate et al. (2016), providing further evidence that they are, in fact, ELMs and their precursors. These objects also lie below the main sequence in the observational H-R diagram (colour-magnitude diagram), shown in Fig. 8.

We find that the (pre-)ELMs in the reliable parallax sample show apparent magnitudes generally fainter than the remaining objects (see Fig. 9). White dwarfs are intrinsically fainter, so that even at relatively high G magnitudes the parallax can be detected.

It is evident in Fig. 7 that ≈ 20 per cent of the objects with radii below the main sequence show $R \approx 0.01 R_{\odot}$, consistent with single-evolution models of canonical mass white dwarfs. However, some of the known ELMs in tight binaries also lie in the region of the single evolution models and still show low estimated masses (e.g. J233821.504-205222.78, with a mass of $0.258 M_{\odot}$, and J115138.378+585853.20, with a mass of $0.186 M_{\odot}$). The objects in our sample were selected for showing narrow hydrogen lines in their spectra that are best fit to low-mass white dwarf models with $\log g \lesssim 6$. We keep the objects with $R \sim 0.01 R_{\odot}$ in Table 1 so that they can be investigated as possible outcomes of binary evolution.

We note that a fraction of these 187 objects are clustered at $T_{\text{eff}} \approx 7000$ K (see Fig. 6). The binary evolution models indicate no physical reason for this clustering. To investigate its possible cause, we repeated our simulation with the uncertainty in the spectroscopic temperature increased artificially to 10 per cent. The slope of minimal radius along the main sequence steepens for $T_{\text{eff}} < 7000$ K, and this increase in the uncertainty allows most of the objects in the clustered region to show radii consistent with the cooler main sequence considering the 99 per cent confidence level. Nevertheless, we have no evidence that our temperatures have an uncertainty higher than 5 per cent. Comparison with other temperature estimates, e.g. from *Gaia* (Andrae et al. 2018), suggest uncertainties of, at most, 6.5 per cent. However, at lower temperatures the external uncertainty of the models does become larger, due to increased uncertainty in the opacities. Hence 10 per cent might be a conservative estimate if these stars are scattered up from intrinsically lower effective temperatures. The 88 objects whose radii are still below the main sequence at 99 per cent confidence after allowing an uncertainty of 10 per cent in T_{eff} are flagged in Table 1.

In our simulations that approximate extinction based on the SDSS magnitudes, 18 per cent of the objects in Table 1 would have inconclusive radii. Given that the extinction map

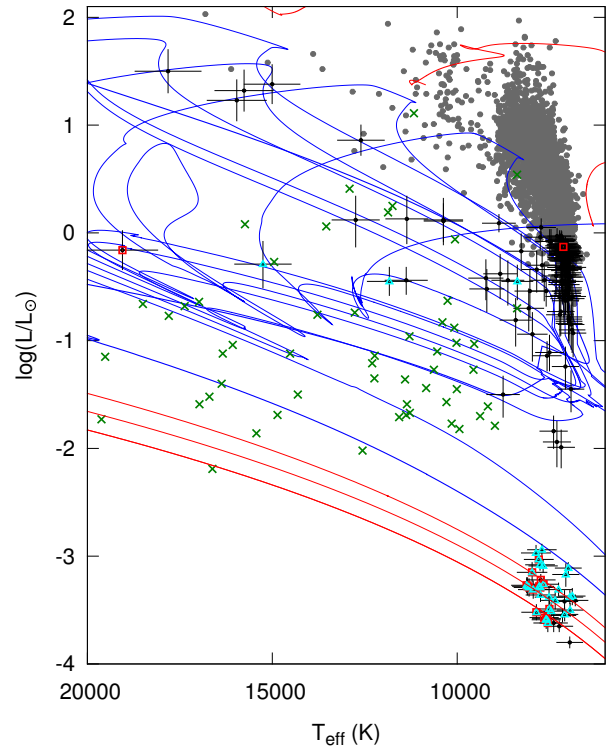


Figure 7. H-R diagram showing the whole reliable parallax π sample as grey dots. The objects with radii smaller than main sequence assuming a 99 per cent confidence interval and 5 per cent uncertainty in T_{eff} are shown in black, with error bars. Objects found to be most likely (pre-)ELMs from Pelisoli et al. (2018a) are marked with cyan triangles, while those with $\log g > 5.5$ are marked with red squares. Blue lines show the binary evolution models of Istrate et al. (2016) for $z = 0.01$ that take rotation into account, ranging from 0.182 (thin) to $0.324 M_{\odot}$ (thick). The location of the (pre-)ELMs agrees well with the region spanned by these models, with the exception of a few canonical-mass white dwarfs. Known ELMs in binaries from table 5 of Brown et al. (2016) are shown as green crosses for comparison. The red lines are single-evolution models computed with the LPCODE (Althaus et al. 2003) for low-metallicity ($z = 0.004$) stars with initial masses of 1.0 , 2.0 , and $3.0 M_{\odot}$ (from top to bottom).

of Schlegel et al. (1998) has low resolution, we preferred to use the radii derived from *Gaia* parameters alone, but we caution that there exists this 18 per cent bias in the number of (pre-)ELMs because of unaccounted-for extinction. The objects that remain smaller than the main sequence in 99% of simulations that include these SDSS extinction estimates are flagged in our table (151 stars). We also flag objects that are convincingly (pre-)ELMs when the systematic parallax uncertainty is added in quadrature to the catalogue uncertainties (73 stars). Our most certain identifications of (pre-)ELMs are the 66 sdAs that remain below the minimum main sequence limit through all three tests of additional systematics.

Table 1. (Pre-)ELMs and some possibly canonical mass white dwarfs identified in the sdA sample. Uncertainties in T_{eff} and $\log g$ are formal fitting errors obtained from the SDSS spectral fit. The radii were calculated from the luminosity derived from Gaia data and our spectroscopic T_{eff} . The flags $F_{T_{\text{eff}}}$, F_{ext} , and F_{sys} mark objects that remain below the main sequence (value = 1) when the T_{eff} uncertainty is increased to 10 per cent, when full extinction correction is applied, and when the systematic uncertainty is added. The complete Table is available online.

SDSS J	T_{eff} (K)	$\log g$	d (pc)	$\sigma_{d_{\text{upper}}}$	$\sigma_{d_{\text{lower}}}$	$R(R_{\odot})$	$\sigma_{R_{\text{upper}}}$	$\sigma_{R_{\text{lower}}}$	$F_{T_{\text{eff}}}$	F_{ext}	F_{sys}
000320.54-103758.4	7194(13)	4.44(0.04)	1703	291	212	0.4483	0.0948	0.0737	0	1	0
000720.18-023456.0	7594(33)	5.82(0.08)	109	6	5	0.0093	0.0013	0.0011	1	1	1
000758.17-024941.8	7650(29)	6.11(0.07)	106	3	3	0.0093	0.0012	0.0011	1	1	1
002105.91-024907.7	7153(42)	7.69(0.07)	117	4	4	0.0109	0.0014	0.0012	1	1	1
002543.80-104706.8	6919(35)	3.87(0.18)	1529	447	286	0.2640	0.0855	0.0559	1	1	0
004001.42+005908.7	7391(34)	5.37(0.10)	128	8	7	0.0095	0.0014	0.0012	1	1	1
005614.07-045750.3	7197(10)	4.54(0.03)	1629	166	138	0.5473	0.0884	0.0709	0	1	0
011039.40-100311.5	7747(41)	4.78(0.22)	149	7	6	0.0117	0.0015	0.0013	1	1	1
012000.11+003251.4	7019(14)	4.21(0.08)	1393	267	193	0.3494	0.0820	0.0601	1	1	1
012416.72+405413.7	15005(105)	4.39(0.02)	2578	320	259	0.7304	0.1954	0.1526	0	1	0

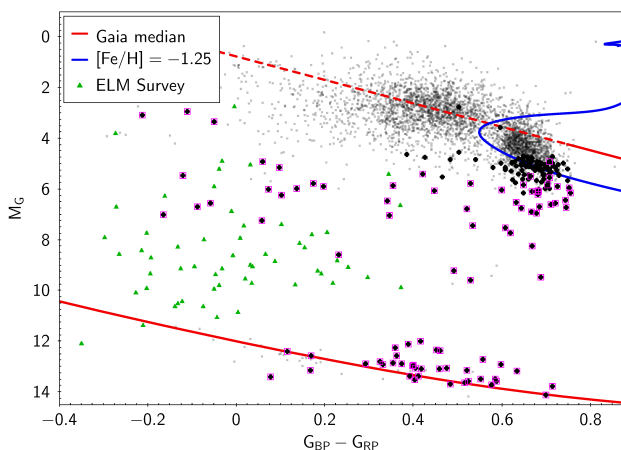


Figure 8. Absolute magnitude M_G and colour $G_{BP} - G_{RP}$ for the reliable π sample as grey dots. The objects with radii smaller than main sequence assuming a 99 per cent confidence interval and 5 per cent uncertainty in T_{eff} are marked with black circles, with those still below the main sequence assuming 10 per cent uncertainty marked with magenta squares. The red lines are the fiducial lines from fig. 8 of Gaia Collaboration et al. (2018), which show the position of the main sequence (top) and white dwarfs (bottom). The dashed portion was extrapolated. The blue line is the MIST isochrone for 10 Gyr and $[\text{Fe}/\text{H}] = -1.25$.

4 DISCUSSION

Most of the objects whose radii are not below the main sequence with 99 per cent confidence show a confidence interval for the radii spanning both above and below the main sequence lower limit, with only 885 (23 per cent) objects showing the 99 per cent confidence level above the main sequence minimum. We cannot make any claims about the nature of individual objects whose radii are not below the ZAMS; they are consistent with both the main sequence and with pre-ELMs, given the occurrence of burning stages that can increase pre-ELM radii above the main sequence, as mentioned above. For example, Liakos (2018) recently found a $0.07 M_{\odot}$ pre-ELM with a $1.0 R_{\odot}$ radius in an Algol-type binary. However, given the short lifetimes of pre-ELMs (only up to the order of a few million years in the models of Istrate et al. 2016), the most likely explanation is that

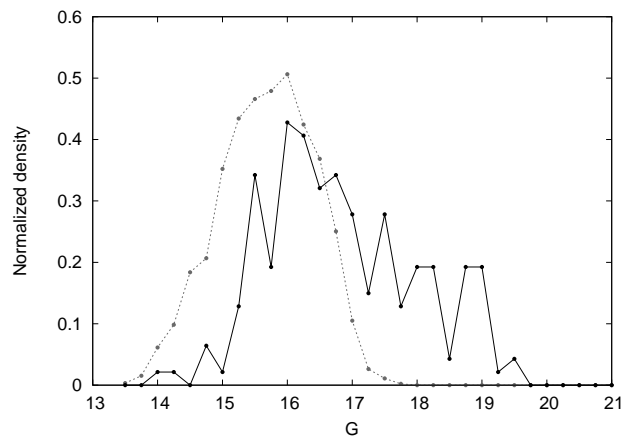


Figure 9. Number density of objects as a function of apparent magnitude G . The black solid line shows objects whose radii are smaller than main sequence, the grey dashed is for the remaining objects in the sample.

the majority of sdAs are simply metal-poor main sequence stars, as already suggested by Brown et al. (2017). The positions of most of these objects in the color-magnitude diagram of Fig. 8 are consistent with MIST isochrones (Dotter 2016; Choi et al. 2016), suggesting that they are metal-poor main sequence stars in the halo, with $M < 0.9 M_{\odot}$ and $6000 < T_{\text{eff}} < 8000$ K. Such physical parameters are very different compared to those of disc A-type stars ($M \gtrsim 2.0 M_{\odot}$, $T_{\text{eff}} \sim 10000$ K): these objects are not bona-fide A stars, they simply mimic hydrogen-line-dominated A-type spectra due to the low metallicity. They likely have masses below $1 M_{\odot}$, corresponding to longer main sequence lifetimes that are consistent with the age of the halo. They are also intrinsically fainter than A stars, hence not saturated in the SDSS for distances down to ~ 2 kpc, consistent with the halo. A significant number of objects (≈ 2200), however, lie bluer than the turnoff—these are possibly blue straggler stars, which are indeed A-type stars and are also believed to be binary byproducts like the ELMs. In this case, the lifetime in the main sequence is extended by mass accretion. A gap between these two populations can be glimpsed in Fig. 8, and its position coincides approximately with the

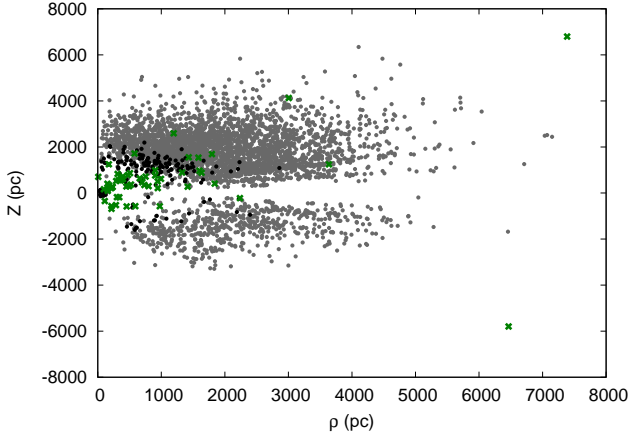


Figure 10. Diagram showing the disc height Z vs. the distance in the Galactic plane $\rho = \sqrt{X^2 + Y^2}$, with same colour coding as previous figures. There are more objects at $Z > 0$ and few close to the disk because of the SDSS coverage of the sky.

turnoff for a metallicity of $[Fe/H] = -1.25$, which is the average metallicity of the analysed sdAs that have SSPP determinations.

Given their smaller-than-main-sequence radii, the distances of the (pre-)ELM objects are consistent with the Galactic disc, as we had already suggested in Pelisoli et al. (2018a). Objects with inconclusive radii extend to larger distances, as expected for a halo population. Fig. 10 shows a diagram of the disc height Z as a function of $\rho = \sqrt{X^2 + Y^2}$. The (pre-)ELMs are all within 3 kpc. SDSS observed only 35 per cent of the sky, and only 40 per cent of white dwarfs were followed up spectroscopically with SDSS (Gentile Fusillo et al. 2015, e.g.); accounting for this, the population is consistent with a thick disc with a scale height of 900 pc (Bland-Hawthorn & Gerhard 2016), as can be seen in the histogram of Fig 11. There is a noticeable bimodality in the Z distribution. This can partially be explained by the possible presence of canonical-mass white dwarfs in the sample, which are intrinsically fainter than (pre-)ELMs and could account for the peak at smaller Z . However, a certain bimodality in the radii of detected (pre-)ELMs can also be explained in terms of their evolution. As previously stated, most of their lives is spent in the cooling sequence with $R \lesssim 0.1 R_{\odot}$, which increases the probability of detection at these small radii. On the other hand, the maximum distance at which a (pre-)ELM can be detected scales with its radius. From the models of Istrate et al. (2016), we obtained that the maximum observable volume becomes the dominant factor for the probability of detection at $R \gtrsim 0.2 R_{\odot}$. Therefore there are two regimes for (pre-)ELM detection: dominated by the large timescales (small radii), or dominated by brightness (large radii). As our initial sample selection took into account the SDSS spectral classification as main sequence A, B or O stars, it should be biased toward the large radii regime, because small radii objects would be most likely classified as white dwarfs by the SDSS pipeline.

The kinematics of the new (pre-)ELMs are harder to parse, as is shown in Fig. 12. The peak is consistent with the disk, but there is a larger tail to high velocities than expected from a disc distribution. The same happens for

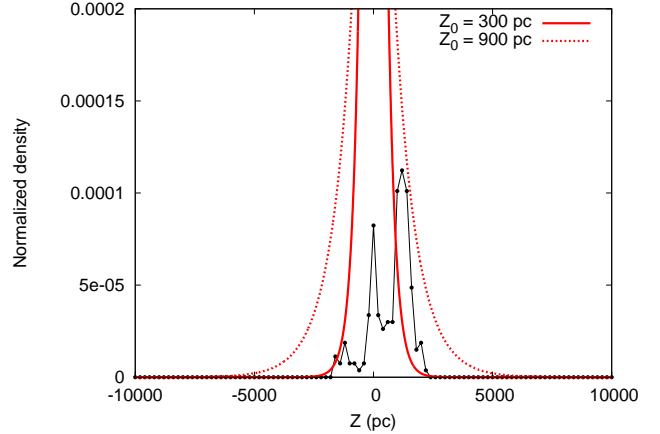


Figure 11. Distribution of disc height for the (pre-)ELMs (black). We have assumed the sample corresponds to 14 per cent fraction of the complete population, considering the 40 per cent rate of spectroscopic follow up for white dwarfs in SDSS (Gentile Fusillo et al. 2015, e.g.) and the SDSS coverage of 35 per cent of the sky. Their distribution is consistent with the disc, assuming the scale heights for thin (300 pc) and thick disc (900 pc) given by Bland-Hawthorn & Gerhard (2016).

the objects whose radii are inconclusive. In the case of the (pre-)ELMs, this can maybe be explained by a contribution of the orbital component to the estimated velocities, given that (pre-)ELMs are most likely of binary origin. For the remaining objects, the larger velocities could be due to a halo population. This is not unexpected, given that much of the disc population of larger stars would be above the saturation limit of the SDSS ($g \approx 14.0$). In fact, over 1550 objects in the sample (40 per cent) show tangential velocity $v_T > 200 \text{ km s}^{-1}$ (the halo selection assumed by Gaia Collaboration et al. 2018). 78 show $v_T > 500 \text{ km s}^{-1}$. Although out of the scope of this work, their nature as possible hypervelocity stars should be investigated. It is important to emphasise again that we cannot rule out that some of these objects could be pre-ELMs, in which case the velocity could be explained by orbital motion, hence the high velocity objects should also be probed as pre-ELMs, regardless of radius.

Fig. 13 shows the normalized number density of the maximum difference in radial velocity between SDSS subspectra, ΔRV , for (pre-)ELMs compared to the remaining sample. The SDSS time coverage and the signal-to-noise ratio of the subspectra are not enough to claim binarity in most cases (Badenes & Maoz 2012), but it can still be noted that the (pre-)ELMs show more objects with high ΔRV , which is expected considering that they are most likely products of binary evolution. However, it is important to notice that the (pre-)ELMs are mostly fainter than the inconclusive objects (see Fig. 9), therefore this could also be due to larger spread resulting from lower signal-to-noise (S/N) spectra. We have analysed only objects whose SDSS final spectra show $S/N > 15$, but the individual subspectra can show significantly lower S/N .

From the 1150 objects identified as most likely (pre-)ELMs by Pelisoli et al. (2018a), 150 were in our reliable π sample, and 54 were found to indeed show radii smaller than the main sequence; most are, however, consis-

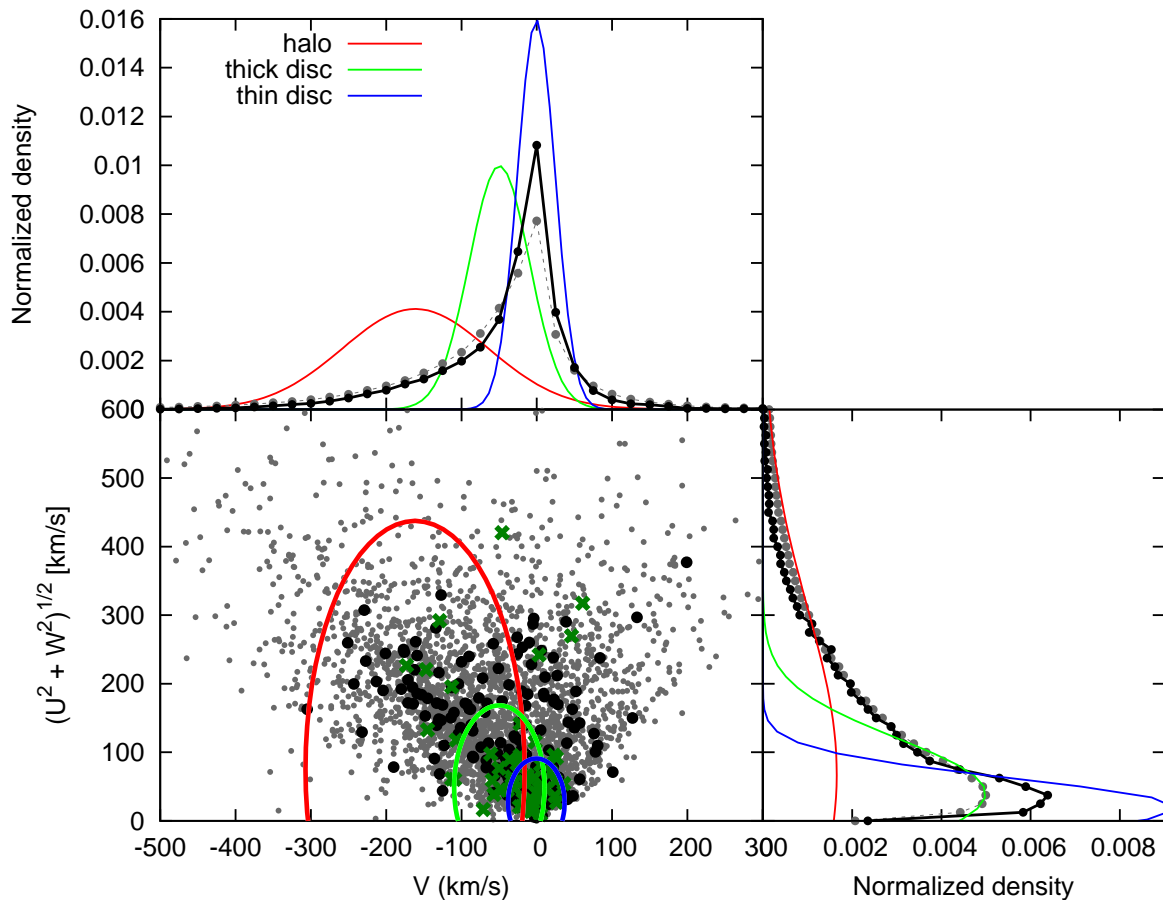


Figure 12. Bottom left panel shows the Toomre diagram following same colour coding for the dots as previous figures. The ellipsoids show the 3σ contours for Galactic thin disc (blue), thick disc (green) and stellar halo (red) populations. The top and bottom right panel show the distributions, again with same colour coding. It can be seen that the distributions peak at the position of disc, but show an extended tail. As the distances suggest that the (pre-)ELMs are within the disc, the tail could be due to an orbital component of the velocity. For the remaining objects, this could imply a halo population, given that they are detected at larger distances.

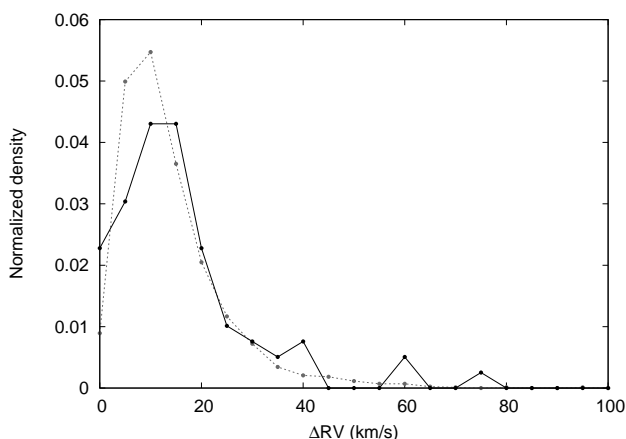


Figure 13. Normalized number density for the maximum difference in radial velocity measured in SDSS subspectra. The black line is for the identified (pre-)ELMs, the dashed grey for the remaining sample. It seems that the (pre-)ELMs show higher velocity amplitudes on average, as expected from a binary evolution origin.

tent with single evolution models. As to the 411 objects with $\log g > 5.5$ from fits to their SDSS spectra, 94 were analysed and we established that 20 show radii below the main sequence. Many are possibly canonical mass white dwarfs, considering their position in the H-R diagram of Fig. 7. As we cannot rule out that the remaining objects are (pre-)ELMs, even if the radii are consistent with main sequence stars, the fact that not all objects were confirmed as (pre-)ELMs should not be interpreted as definitive. It is interesting to notice, however, that most of the identified (pre-)ELMs are concentrated at low T_{eff} (see Fig. 7), contrary to our prediction in Pelisoli et al. (2018a) that they would be more common in the hot population. As the nature of most objects still remains uncertain, further conclusions on the T_{eff} as a determining factor on the evolutionary origin of the sdAs cannot be drawn. In Appendix A, we show a comparison between the distances and proper motions quoted in the work of Pelisoli et al. (2018a) compared with the updated values from *Gaia*.

We suggested in Pelisoli et al. (2018a) that at least ≈ 7 per cent of the sdAs are (pre-)ELMs. This matches approximately the fraction of sdAs determined to be (pre-)ELMs

smaller than the main sequence limit to $> 99\%$ certainty; however, a direct comparison is not possible due to complicated selection effects of the astrometric sample.

5 SUMMARY AND CONCLUSIONS

The evolutionary origin of the sdAs has been elusive since their discovery by Kepler et al. (2016). It has always been emphasised how *Gaia* would be able to shed light on the issue. We analysed the sample of sdAs previously published in Pelisoli et al. (2018a) in light of *Gaia* DR2 data. While parallaxes are unreliable considering our selection criteria for 90 per cent of the sample, we were able to identify 187 new high-probability (pre-)ELMs among the 3891 sdAs with reliable *Gaia* parallaxes. These identifications increase the number of known (pre-)ELMs by up to a factor of three. We consider 66 of these to be most reliably compact objects since they remain below the main sequence when we include an approximate treatment of extinction and inflate the uncertainties on T_{eff} and parallax. The nature of the remaining objects in the sample is still unconfirmed with the *Gaia* parallaxes, but their position in the HR diagram supports that most are consistent with a population of low-metallicity main sequence stars in the halo, as first suggested by Brown et al. (2017), with contributions from a low-mass ($M \lesssim 0.9 M_{\odot}$) population and from a population of blue straggler stars.

The position of the discovered (pre-)ELMs coincides well with the region of the H-R diagram spanned by the binary evolution models of Istrate et al. (2016). This supports a binary evolution origin for the (pre-)ELMs. In fact, we have also noticed that these objects show a distribution of RV amplitudes in the SDSS subspectra shifted to higher values when compared to the other objects in the sample. Yet some show low RV dispersion, hence individual systems cannot be ruled out as single. Although the (pre-)ELMs are more easily explained as having been created in multiple systems, this does not imply that they are currently in close binaries, similarly to the hot subdwarfs sDBs/sdOs (e.g. Heber 2016); as mentioned in the Introduction, alternative explanations have been put forward. Time-resolved spectroscopy of the objects in this sample should be obtained so that the present binary ratio of the (pre-)ELMs can be accurately determined.

As already noted in our previous works (Pelisoli et al. 2017, 2018a), the (pre-)ELM radii give the sdAs a distribution of distances consistent with the Galactic disc. The velocities are ambiguous—the peak is consistent with the disc, but the tail extends to larger velocities. This can possibly be explained by orbital motion. The remaining objects still show larger distances, with the velocities indicating that a halo contribution is required. Almost a hundred of these show $v_T > 500 \text{ km s}^{-1}$ and could be high velocity stars.

The new (pre-)ELMs show temperatures cooler than the bulk of known ELMs (which mostly have $T_{\text{eff}} \gtrsim 10\,000 \text{ K}$; e.g., Brown et al. 2016). We have previously raised the issue of a missing, cooler population (Pelisoli et al. 2018a), and pointed out that this missing population was most likely within the sdAs, which is now confirmed.

These identifications likely correspond to only a fraction of the (pre-)ELMs within the larger sdA sample, given our conservative choice of minimal main-sequence radius. The

average value of $[\text{Fe}/\text{H}]$ for the analysed sdAs fitted by SSPP is -1.33 , with a spread of 0.84 , whereas we have assumed a value of $[\text{Fe}/\text{H}] = -4.0$ to determine the minimum radius. Assuming a higher metallicity would increase the minimum radius limit and the number of objects with radii below it. On the other hand, the number of identifications decreases by 18 per cent when we include an estimate of extinction based on SDSS magnitudes, and by 60 per cent when the *Gaia* systematics are added to the uncertainty in parallax.

Our work demonstrates the potential of using *Gaia* to identify new (pre-)ELMs. Future data releases will further improve our understanding of the sdAs and how they fit into our theories of stellar evolution and Galaxy structure and formation. In particular, *Gaia* radial velocities from multiple epochs will enable better constraints on binarity, as would follow-up ground-based spectroscopy. Improved extinction maps would reduce uncertainties in our radius estimates, allowing us to better separate different luminosity classes. Searches independent of the SDSS identifications should be done to provide an unbiased catalogue of (pre-)ELMs (similar to the approach used to identify white dwarfs in *Gaia* data by Kilic et al. 2018; Gentile Fusillo et al. 2018). An unbiased catalogue could help constrain the evolutionary timescales during the pre-ELM phase compared to the cooling-track phases. The predictions from theoretical models are largely affected by uncertainties on residual burning rates. A magnitude-limited sample would also better reveal the Galactic location and kinematics of the sdA subpopulations. Identifications of (pre-)ELMs in the pulsational instability strips can also inform efforts to astroseismically constrain the interiors of post-common-envelope mass-transfer remnants in a regime where spectroscopic classifications have not been reliable (Bell et al. 2017). Such studies will not only improve our understanding of the formation of the ELMs themselves, but also of binary evolution as a whole.

ACKNOWLEDGEMENTS

IP and SOK acknowledge support from CNPq-Brazil. DK received support from programme Science without Borders, MCIT/MEC-Brazil. IP was also supported by Capes-Brazil under grant 88881.134990/2016-01, and by DFG under grant GE 2056-12-1. KJB was supported by the European Research Council under the European Community's Seventh Framework Programme (FP7/2007-2013) / ERC grant agreement no 338251 (StellarAges). We thank Warren Brown, Mukremin Kilic, JJ Hermes, and Saskia Hekker for reading the draft of this work and providing helpful comments, and Alejandra D. Romero for providing single evolution models. We also thank Stefan Jordan, Uli Bastian, and the organizers and participants of the *Gaia* Data Workshop held in Heidelberg for useful discussions.

This work has made use of data from the European Space Agency (ESA) mission *Gaia* (<https://www.cosmos.esa.int/gaia>), processed by the *Gaia* Data Processing and Analysis Consortium (DPAC, <https://www.cosmos.esa.int/web/gaia/dpac/consortium>). Funding for the DPAC has been provided by national institutions, in particular the institutions participating in the *Gaia* Multilateral Agreement.

REFERENCES

- Althaus L. G., Serenelli A. M., Córscico A. H., Montgomery M. H., 2003, *A&A*, **404**, 593
- Althaus L. G., Miller Bertolami M. M., Córscico A. H., 2013, *A&A*, **557**, A19
- Andrae R., et al., 2018, preprint, ([arXiv:1804.09374](https://arxiv.org/abs/1804.09374))
- Badenes C., Maoz D., 2012, *ApJ*, **749**, L11
- Bailer-Jones C. A. L., 2015, *PASP*, **127**, 994
- Bailer-Jones C. A. L., Rybizki J., Fouesneau M., Mantelet G., Andrae R., 2018, preprint, ([arXiv:1804.10121](https://arxiv.org/abs/1804.10121))
- Bell K. J., et al., 2017, *ApJ*, **835**, 180
- Bell K. J., et al., 2018, preprint, ([arXiv:1805.11129](https://arxiv.org/abs/1805.11129))
- Bertelli G., Girardi L., Marigo P., Nasi E., 2008, *A&A*, **484**, 815
- Bertelli G., Nasi E., Girardi L., Marigo P., 2009, *A&A*, **508**, 355
- Bland-Hawthorn J., Gerhard O., 2016, *ARA&A*, **54**, 529
- Brown W. R., Kilic M., Allende Prieto C., Kenyon S. J., 2010, *ApJ*, **723**, 1072
- Brown W. R., Kilic M., Allende Prieto C., Kenyon S. J., 2012, *ApJ*, **744**, 142
- Brown W. R., Kilic M., Allende Prieto C., Gianninas A., Kenyon S. J., 2013, *ApJ*, **769**, 66
- Brown W. R., Gianninas A., Kilic M., Kenyon S. J., Allende Prieto C., 2016, *ApJ*, **818**, 155
- Brown W. R., Kilic M., Gianninas A., 2017, *ApJ*, **839**, 23
- Choi J., Dotter A., Conroy C., Cantiello M., Paxton B., Johnson B. D., 2016, *ApJ*, **823**, 102
- Dotter A., 2016, *ApJS*, **222**, 8
- Duchêne G., Kraus A., 2013, *ARA&A*, **51**, 269
- Evans D. W., et al., 2018, preprint, ([arXiv:1804.09368](https://arxiv.org/abs/1804.09368))
- Gaia Collaboration et al., 2018, preprint, ([arXiv:1804.09378](https://arxiv.org/abs/1804.09378))
- Gentile Fusillo N. P., Gänsicke B. T., Greiss S., 2015, *MNRAS*, **448**, 2260
- Gentile Fusillo N. P., et al., 2018, preprint, ([arXiv:1807.03315](https://arxiv.org/abs/1807.03315))
- Gianninas A., Kilic M., Brown W. R., Canton P., Kenyon S. J., 2015, *ApJ*, **812**, 167
- Heber U., 2016, *PASP*, **128**, 082001
- Hermes J. J., Gänsicke B. T., Breedt E., 2017, in Tremblay P.-E., Gänsicke B., Marsh T., eds, *Astronomical Society of the Pacific Conference Series Vol. 509, 20th European White Dwarf Workshop*. p. 453 ([arXiv:1702.07370](https://arxiv.org/abs/1702.07370))
- Istrate A. G., Marchant P., Tauris T. M., Langer N., Stancliffe R. J., Grassitelli L., 2016, *A&A*, **595**, A35
- Johnson D. R. H., Soderblom D. R., 1987, *AJ*, **93**, 864
- Jordi C., et al., 2010, *A&A*, **523**
- Kepler S. O., et al., 2016, *MNRAS*, **455**, 3413
- Kilic M., Stanek K. Z., Pinsonneault M. H., 2007, *ApJ*, **671**, 761
- Kilic M., Brown W. R., Allende Prieto C., Agüeros M. A., Heinke C., Kenyon S. J., 2011, *ApJ*, **727**, 3
- Kilic M., Brown W. R., Allende Prieto C., Kenyon S. J., Heinke C. O., Agüeros M. A., Kleinman S. J., 2012, *ApJ*, **751**, 141
- Kilic M., et al., 2014, *MNRAS*, **438**, L26
- Kilic M., Hambly N. C., Bergeron P., Rowell N., 2018, preprint, ([arXiv:1805.01227](https://arxiv.org/abs/1805.01227))
- Kleinman S. J., et al., 2013, *ApJS*, **204**, 5
- Lee Y. S., et al., 2008, *AJ*, **136**, 2022
- Liakos A., 2018, preprint, ([arXiv:1805.00798](https://arxiv.org/abs/1805.00798))
- Lindegren L., et al., 2018, preprint, ([arXiv:1804.09366](https://arxiv.org/abs/1804.09366))
- Luri X., et al., 2018, preprint, ([arXiv:1804.09376](https://arxiv.org/abs/1804.09376))
- Marsh T. R., Dhillon V. S., Duck S. R., 1995, *MNRAS*, **275**, 828
- Maxted P. F. L., et al., 2011, *MNRAS*, **418**, 1156
- Nelemans G., Tauris T. M., 1998, *A&A*, **335**, L85
- Nelemans G., Yungelson L. R., Portegies Zwart S. F., Verbunt F., 2001, *A&A*, **365**, 491
- Pelisoli I., Kepler S. O., Koester D., 2017, *Open Astronomy*, **26**, 169
- Pelisoli I., Kepler S. O., Koester D., 2018a, *MNRAS*, **475**, 2480
- Pelisoli I., Kepler S. O., Koester D., Castanheira B. G., Romero A. D., Fraga L., 2018b, *MNRAS*, **478**, 867
- Pietrzyński G., et al., 2012, *Nature*, **484**, 75
- Postnov K. A., Yungelson L. R., 2014, *Living Reviews in Relativity*, **17**, 3
- Rappaport S., Nelson L., Levine A., Sanchis-Ojeda R., Gandolfi D., Nowak G., Palle E., Prsa A., 2015, *ApJ*, **803**, 82
- Romero A. D., Campos F., Kepler S. O., 2015, *MNRAS*, **450**, 3708
- Schlegel D. J., Finkbeiner D. P., Davis M., 1998, *ApJ*, **500**, 525
- Tian H.-J., et al., 2017, *ApJS*, **232**, 4
- Toonen S., Hamers A., Portegies Zwart S., 2016, *Computational Astrophysics and Cosmology*, **3**, 6
- Vos J., Zorotovic M., Vučković M., Schreiber M. R., Østensen R., 2018, *MNRAS*,
- Wang B., Han Z., 2009, *A&A*, **508**, L27
- Willems B., Kolb U., 2004, *A&A*, **419**, 1057
- Zinn J. C., Pinsonneault M. H., Huber D., Stello D., 2018, preprint, ([arXiv:1805.02650](https://arxiv.org/abs/1805.02650))

APPENDIX A: COMPARISON WITH PREVIOUS DATA

Fig. A1 compares the distances obtained from the *Gaia* parallaxes with our previous values calculated from the solid angles and radii estimates. For the (pre-)ELMs, we show the distance that we derived given the radii interpolated from the models of Althaus et al. (2013) using our spectroscopic $\log g$. For a significant number of objects, the distance was underestimated by a factor of ten, which is consistent with the systematic uncertainty of -0.5 to -1.0 dex that we found our $\log g$ values determined from SDSS spectra to show (Pelisoli et al. 2018b). This could also be explained if the radii inferred from the models are smaller than the actual radii, implying an underestimate of the distance. For the remaining objects, the distance was obtained assuming a radius interpolated from solar abundance main sequence models given the T_{eff} . In this case, the agreement seems better, given that our T_{eff} is reliable to 5 per cent.

In Fig. A2, we compare the proper motions used in Pelisoli et al. (2018a), obtained from the GPS1 catalogue (Tian et al. 2017) with the new estimates from *Gaia*. The proper motions agree within 3σ for 98 per cent of the sample. As we relied in proper motions, but not on the distance estimates in Pelisoli et al. (2018a), our conclusions then remain unaltered, and are in fact corroborated by this present work: the sdAs are composed of overlapping populations, and at least about 5 per cent of them are (pre-)ELMs.

This paper has been typeset from a $\text{\TeX}/\text{\LaTeX}$ file prepared by the author.

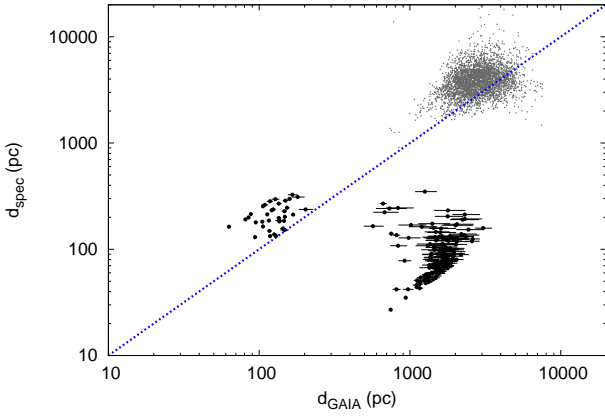


Figure A1. Comparison between the distances estimated from the spectroscopic fits and from *Gaia* parallaxes, for the (pre-)ELMs (black) and for the remaining sample (grey). For the (pre-)ELMs, the radii were estimated relying on the $\log g$, which we found to show a 0.5–1.0 dex uncertainty (Pelisoli et al. 2018b), explaining the cloud of objects with distance underestimated by a factor of ten. For the remaining objects, we show the distance obtained from the solid angle, assuming a main sequence radius interpolated given the fitted T_{eff} . There is relatively good agreement with the *Gaia* estimate in this case.

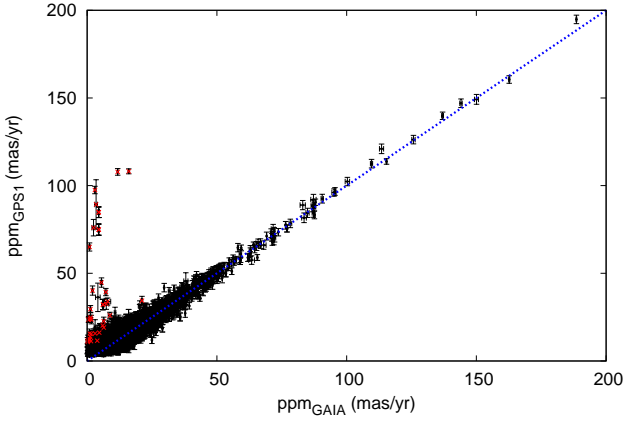


Figure A2. Comparison between the proper motions given in *Gaia* and those of the GPS1 catalogue (Tian et al. 2017), used in Pelisoli et al. (2018a). Objects marked with red crosses show proper motion different between the two catalogues to a 5σ level. Two per cent of the GPS1 proper motions for this sample are overestimated in a 3σ level.